PNAS
www.pnas.org

Supplementary Information for
Characterization of the Strain Rate-Dependent Mechanical Response of Single Cell-Cell Junctions

Amir Monemian Esfahani, Jordan Rosenbohm, Bahareh Tajvidi Safa, Nickolay V. Lavrik, Grayson Minnick, Quan Zhou, Fang Kong, Xiaowei Jin, Eunju Kim, Ying Liu, Yongfeng Lu, Jung Yul Lim, James K. Wahl, Ming Dao, Changjin Huang, Ruiguo Yang

Nickolay V. Lavrik
Email: lavriknv@ornl.org

Ming Dao
Email: mingdao@mit.edu

Changjin Huang
Email: cjhuang@ntu.edu.sg

Ruiguo Yang
Email: ryang6@unl.edu

This PDF file includes:

Supplementary text
Figures S1 to S14
Tables S1
Legends for Movies S1 to S4

Other supplementary materials for this manuscript include the following:

Movies S1 to S4

Supplementary Information Text and Figures

1. System configuration

We used the AFM setup as a tool to stretch the platform. Specifically, we utilized its precise X, Y, and Z positioning capabilities to capture the pillar on the device within a hole drilled into the tip of a cantilever probe tip, and could subsequently define a path for the tip to follow at a specified speed to apply strain at a controlled strain rate to the platform. We did not use any other functions such as spectroscopy. To help illustrate how the AFM setup is integrated into our platform, we drew a Solidworks model as shown in **Fig. S1**.

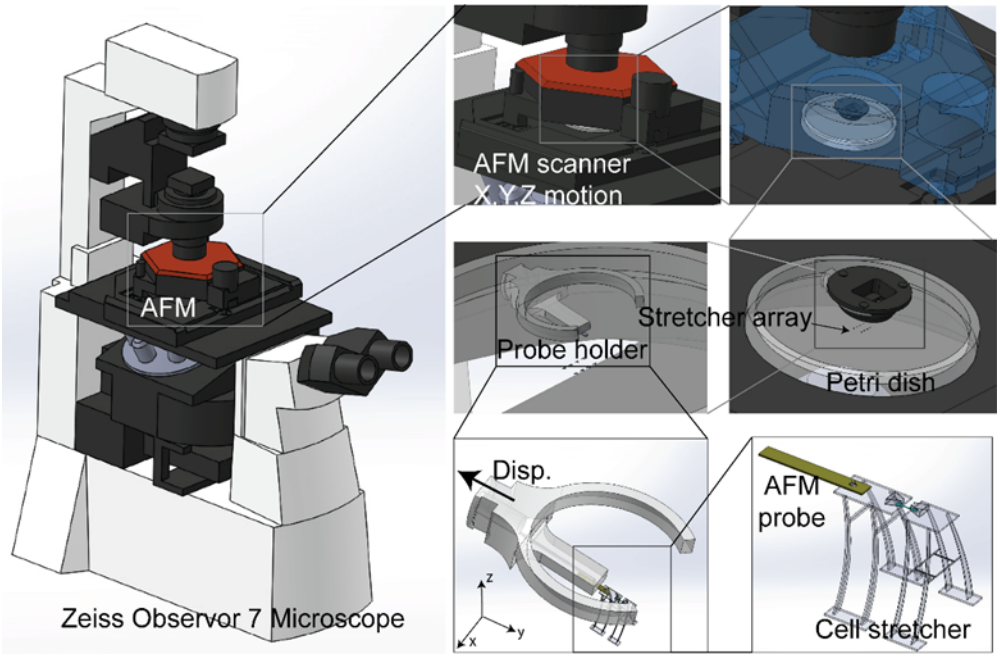

Fig. S1. Detailed illustration of the entire SCAμTT platform. An AFM probe with a hole drilled in the tip with a focused ion beam (FIB) is mounted on the scanner head, and the AFM system is then placed on the stage of an inverted microscope above the sample. The probe tip is then moved using controls on the stage and the AFM software until the pillar is captured within the hole on the probe tip. From here, a line for the probe tip to follow is defined within the AFM software along with the scanning speed to displace the tip in the Y-direction and apply the strain at a controlled strain rate.

2. Design, simulation, and fabrication of the single cell stretcher structure

Several generations of the sensing beam structure have been designed, fabricated, and tested, and their stiffness was calculated using COMSOL Multiphysics simulation software. The first generation was a group of parallel horizontal beams. A design with 5 sets of beams was proposed as the first design. After the simulation, the calculated stiffness was K = 1e5 N/m, which, compared to biological samples, was too large to measure the stress in the cell-cell junction (**Fig. S2a**). By reducing the number of beams, decreasing the beam width from 5 μm to 2.5 μm, and increasing the beam length from 80 μm to 150 μm, we were able to decrease the stiffness to 4.6 N/m (**Fig. S2b**). However, this was still too large to measure stress. Since we reached the maximum printing dimensions of the 3D printer device without stitching, we could not increase the length and due to the structure stability, we could not decrease the width of the beams. A serpentine beam was then proposed to further decrease the stiffness with these geometric constraints in mind. This design further reduced the stiffness of the structure (K = 1.05 N/m) but was still too stiff. (**Fig. S2c**). The force-displacement curves of these designs are compared in **Fig. S2d**. It is worth mentioning that these stiffness data are all calculated in air.

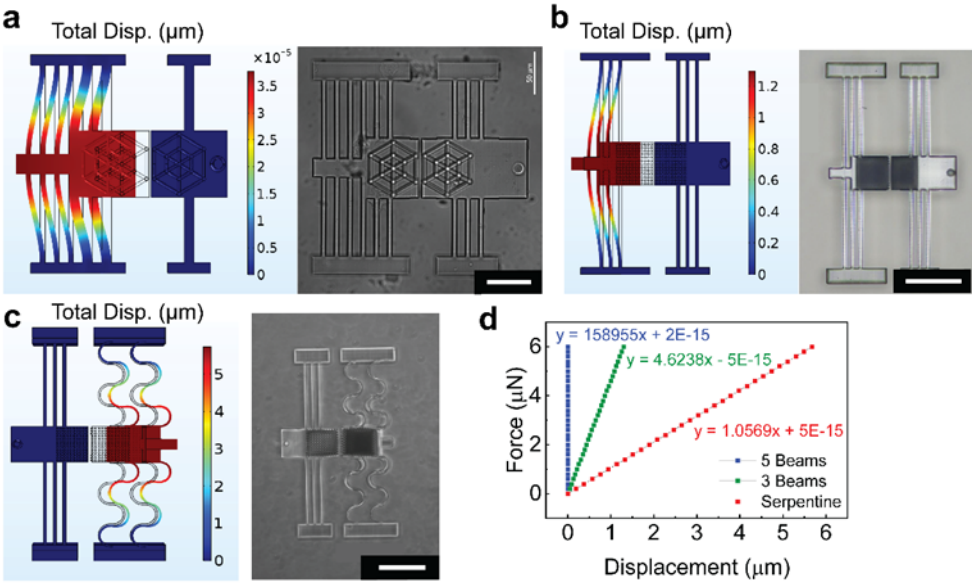

Fig. S2. Design, simulation, and fabrication of the first generation of the single cell pair stretcher (horizontal). **a.** Horizontal beam design with 5 parallel beams attached to the sensing island and 1 pair of beams attached to the actuating island. This design had the highest stiffness (K = 1e5 N/m) and was not able to measure the junction stress. Scale bar = 50 μm. **b.** Horizontal beam design with 3 pairs of beams attached to the sensing and actuating islands, with the width decreased from 5 μm to 2.5 μm and length increased from 80 μm to 150 μm. The new stiffness was 4.6 N/m which is not low enough to measure the junction stress. Scale bar = 100 μm. **c.** Horizontal beam design in which the sensing island beams are changed from the straight to the serpentine design which is less stiff. This design had 1.05 N/m stiffness which is still too stiff to measure the junction stress. Scale bar = 100 μm. **d.** The force versus displacement of different designs has been plotted to compare and find their stiffness.

All of the horizontal beam designs have a stiffness higher than our desired values (0.01 N/m – 0.5 N/m). So, a vertical beam design was proposed (**Fig. S3a**). The vertical beam with a height of 280 μm was able to give us a stiffness close to our goal (0.22 N/m). However, the beams being exactly underneath the islands creates high-intensity background noise during fluorescent imaging, blocking the signal from cells. Therefore, we designed a double cantilever beam design by moving the beams' bases to the sides of the islands (single Λ-shape). Theoretically, this change resulted in increasing the stiffness, so the design was modified by decreasing the beam thickness from 5 μm to 2.5 μm and increasing its height to 300 μm. With COMSOL simulation, its stiffness is lower than the other beam geometry designs (0.08 N/m); however, it collapsed during fabrication. Adding

another set of Λ-shape beams (double Λ-shape) to increase stability still resulted in the collapse of the structures (**Fig. S3b**). Finally, a set of trusses were added horizontally to connect the vertical beams and enhance stability (stabilized A-shape), while decreasing the beam thickness to 2 μm, resulting in stable structures with a stiffness of 0.11 N/m. (**Fig. S3c, d**). It is worth mentioning that these stiffness data are all calculated in air.

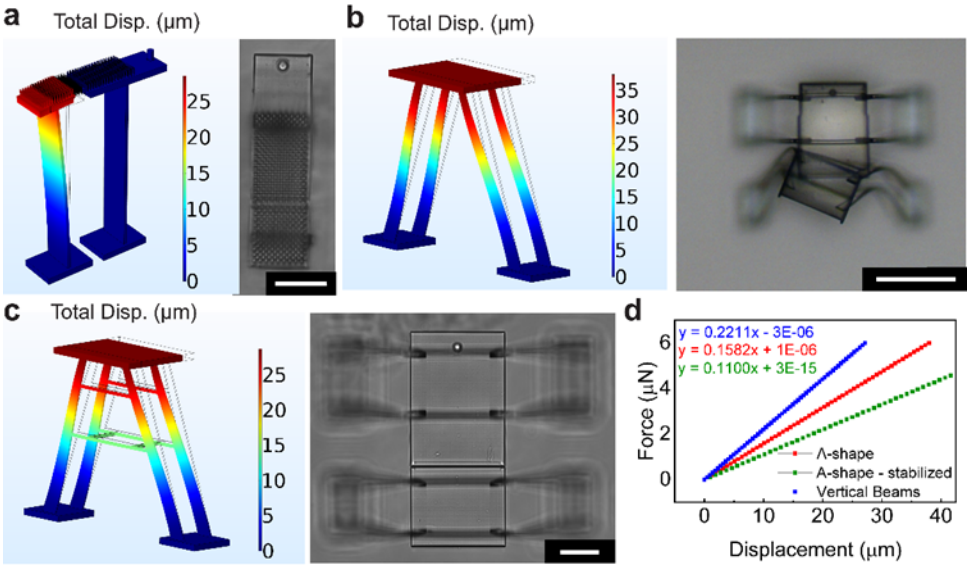

Fig. S3. Design, simulation, and fabrication of the second generation of the single cell pair stretcher (vertical). a. The vertical beam design was less stiff compared to the horizontal beam design and more stable during fabrication. The new design had a height of 280 μm and its stiffness was 0.22 N/m, which allows us to measure the junction stiffness. Scale bar = 50 μm. **b.** The double Λ-shape design solved the background noise issue but it was not stable during fabrication and collapsed. Scale bar = 100 μm. **c.** The double A-shape design with the supporting truss was the final design because of its stiffness and stability. Scale bar = 50 μm. **d.** The force versus displacement of the vertical beam designs has been plotted to compare and find their stiffness.

3. Beam stiffness calculation and calibration

To measure the cell-cell adhesion forces, the mechanical characteristics of the sensing mechanism must be well understood. The modulus of elasticity of TPP fabricated materials varies with laser power, print speed, and post process curing methods. In this study, fabrication parameters remained as consistent as possible. This section highlights the methods used to test, calibrate, and verify the stiffness of the sensing structure mechanism to determine the adhesion forces associated with cell stretching. To do this, a Nanosurf AFM was used to conduct force spectroscopy experiments on horizontally printed sensing microstructures to attain an average stiffness value.

As mentioned in the paper, a tipless cantilever probe (TL-NCL by Nanosensors) with a known and thermally tuned stiffness, k_p, was used to press on horizontally fabricated sensing microstructures with beam thickness, $t = 2\ \mu m$ (**Fig. 1e**). AFM uses the deflection of the probe, Δx_p, and its known stiffness, k_p, to measure the applied force, P_{AFM}. The sensing microstructure is also subjected to the same force as it produces the reaction to cause the probe deflection:

$$P_{AFM} = \Delta x_p \cdot k_p = \Delta x_{sens} \cdot k_{sens} \tag{S1}$$

Here, Δx_{sens} and k_{sens} are the deflection and stiffness of the sensing microstructure, respectively. The AFM outputs the data as force, P_{AFM}, versus displacement, d (**Fig. 1f**). As shown in **Fig. 1e**, the probe is deflected upwards and the structure downwards, therefore the deflection of the microstructure can be calculated by the following:

$$\Delta x_{sens} = d - \Delta x_p \tag{S2}$$

To evaluate the data to find the stiffness, the probe deflection is first found from Eqn. (S1). Next, the structure deflection is solved using Eqn. (S2). Lastly, by substituting the values into the sensing part of Eqn. (S1), the stiffness can be found:

$$k_{sens} = \frac{P_{AFM}}{\Delta x_{sens}} = \frac{1}{d/P_{AFM} - 1/k_p} \tag{S3}$$

To analyze the AFM data, a MATLAB script was used to smooth and average the AFM force versus deflection curves and to calculate the sensing structure stiffness by fitting the averaged line of the data, where the slope was equal to the stiffness.

4. Elastic deformation of the structure

To examine the elasticity of the structure, two experiments were performed with a controlled displacement and release. The first one was a 25 μm displacement and sudden release of the structure and the second one was a 50 μm displacement and sudden release. Since lower strain rates have more impact on the viscoelastic properties of the material, we used 100 nm/s (0.005 s^{-1}) for both experiments. **Fig. S4** shows the displacement-time plots for the experiments. For the 25 μm displacement, 0.135 seconds after release, and for the 50 μm displacement, after 4.72 seconds, both return to the original position within the resolving power of the DIC, thus ruling out major plastic deformation. Further, the rapid release and return of the 25 μm test demonstrate that the viscoelastic effect can be negligible with this displacement, slightly less so with the 50 μm test. In our cell stretch experiments, the displacement of the sensing island is within 5 μm, in which elastic deformation dominates according to this experiment.

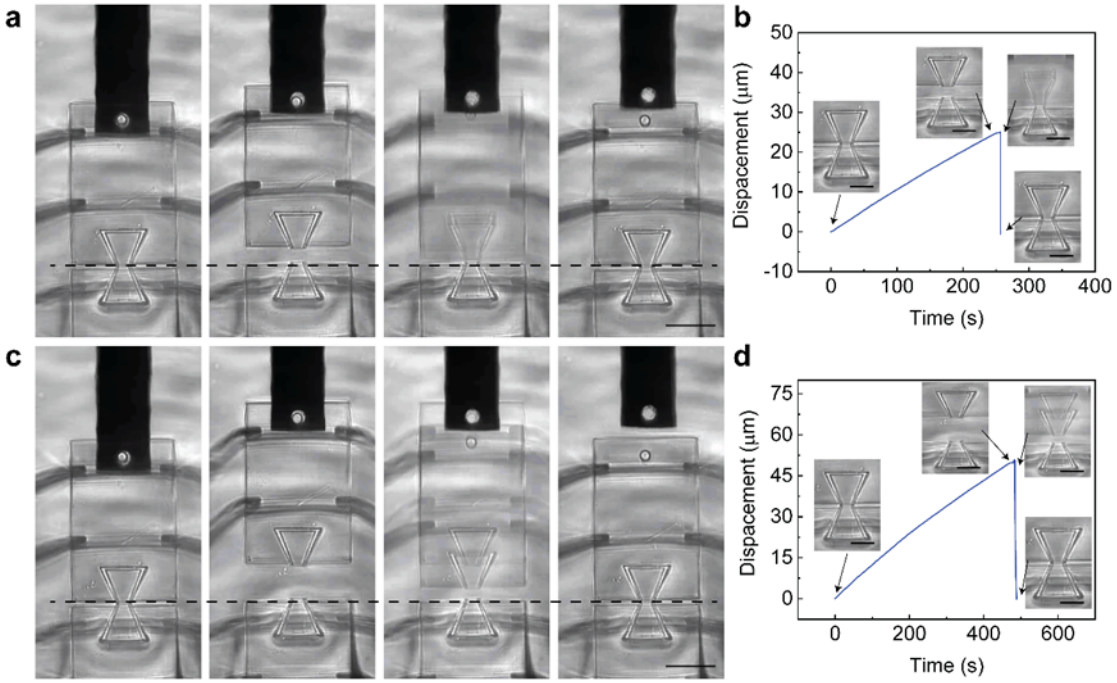

Fig. S4. Elastic deformation of the structure. a. 25 μm displacement and sudden release. Scale bar: 50 μm. **b.** Displacement versus time for the 25 μm displacement. Scale bar: 25 μm. **c.** 50 μm displacement and sudden release. Scale bar: 50 μm. **d.** Displacement versus time for the 50 μm displacement. Scale bar: 25 μm.

5. Cell deposition procedure

Cell manipulation was performed using the well-known Eppendorf cell isolation system. This setup consists of a microcapillary (Piezo Drill Tip ICSI, Eppendorf) integrated with a pressure controller (CellTram® 4r Air/Oil, Eppendorf) and a 3D manipulator (TransferMan® 4r, Eppendorf), allowing for precise 3D cell manipulation. The inner diameter of the microcapillary was chosen based on the cell diameter (approximately 15 µm). To aspirate and hold a cell on the needle tip, the inner diameter should be less than the cell diameter. Based on available needle sizes from Eppendorf, we selected Piezo Drill Tip ICSI with 6 µm inner diameter. The needle is connected to the capillary and through a tube to the pressure controller. The tube is filled with mineral oil, and a small displacement of the pressure controller cylinder creates a positive or negative pressure at the needle tip. The needle approaches the cell using the 3D manipulator (**Fig. S5a**). When it touches the cell membrane, a negative pressure is applied to aspirate the cell (**Fig. S5b**). While the cell is held at the needle tip, it is positioned above Island 2, and a positive pressure is applied to detach the cell from the needle and place it on the surface (**Fig. S5c**). The same procedures are performed to place the second cell on Island 1 (**Fig. S5d, e, and f**). This process is performed inside a temperature-controlled chamber.

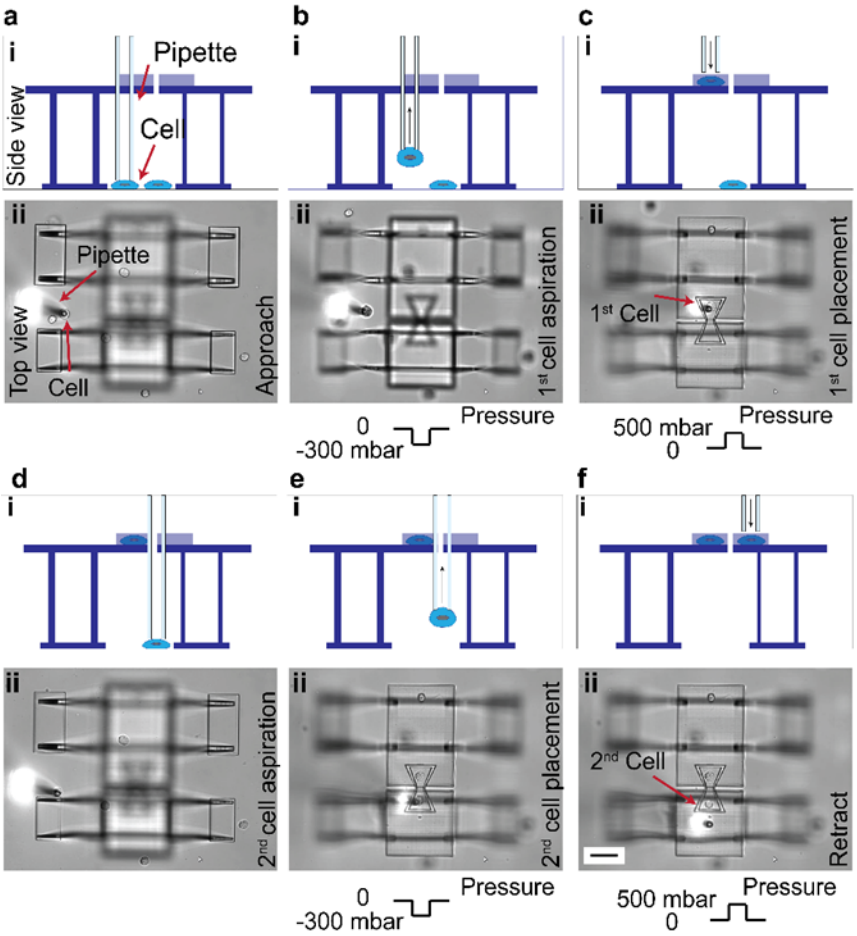

Fig. S5. Cell deposition procedure. a. One cell is targeted and the microcapillary approaches the cell using the 3D manipulator. **b.** A negative pressure is applied with the pressure controller to aspirate and hold the cell. **c.** The manipulator moves the cell to the structure and a positive pressure is applied to deposit the cell on one of the islands. **d-f.** The same steps are performed to aspirate and deposit the second cell on the other island.

6. Cell-cell junction separation under stretch test

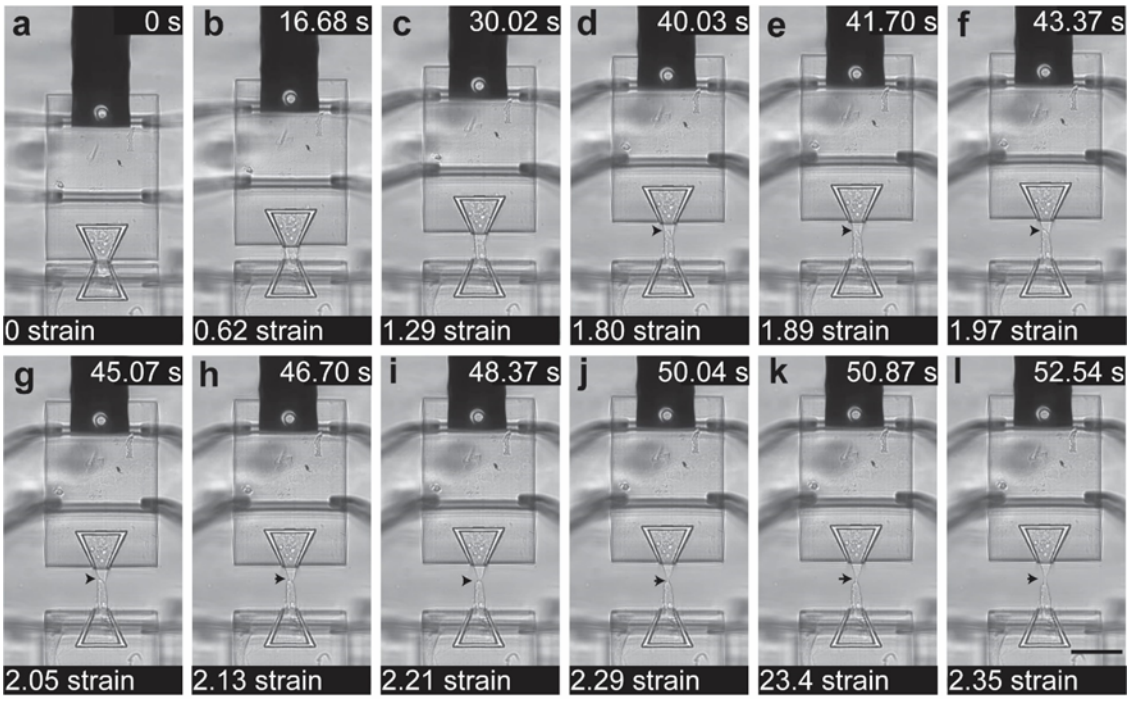

Fig. S6. A representative time-lapse series of frames show the cell junction ruptured symmetrically under an increasing strain. The arrowhead indicates the cell-cell junction in each frame. Scale bar: 20 μm.

7. Standard linear solid model fitting

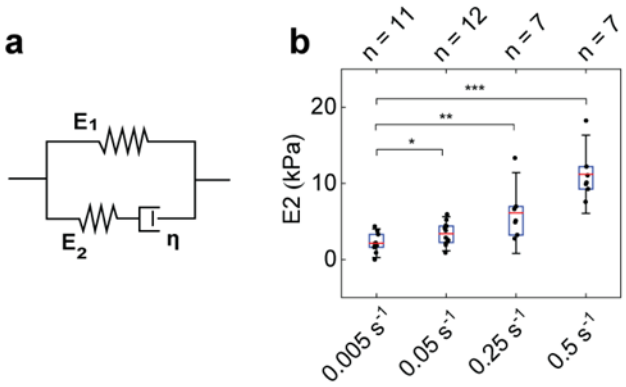

Fig. S7. Fitting the stress-strain curves with the Standard Linear Solid (SLS) model. a. Diagram of the SLS model. **b.** The predicted spring constant E_2 as a function of the strain rate. The equation for the SLS model: $\dot{\sigma}_{tot} + \frac{E_2}{\eta}\sigma_{tot} = \frac{E_1 E_2}{\eta}\varepsilon_{tot} + (E_1 + E_2)\dot{\varepsilon}_{tot}$ can be solved for a constant strain rate: $\sigma_{tot} = \eta\dot{\varepsilon}_{tot}\,(1 - e^{\left(-\frac{E_2}{\eta}t\right)}) + E_1\varepsilon_{tot}$. This equation was used to fit the stress-strain curves at strain rates: 0.005 s^{-1}, 0.05 s^{-1}, 0.25 s^{-1} and 0.5 s^{-1}. The fitting curves are similar to the ones with MSLS fitting in Figure 4b-c. The fitting process yields a relationship between E_2 and strain rate in (b), which shows Young's modulus of the intracellular components, primarily the cytoskeleton, increases significantly with the increase in strain rate. This prediction is clearly in contradiction to the fact that cytoskeleton growth is limited in tests at high strain rates due to the limited response time.

8. CN01, control DMSO, and bleb stretch test frames

Investigation of cellular contractility was performed using CN01, control DMSO, and Bleb with a 0.005 s^{-1} (100 nm/s) strain rate, and representative frames are shown in **Fig. S8**. Control DMSO compared to control at 0.005 s^{-1} showed a sign of rupture because of DMSO (**Fig. S8a**). CN01 increased the stress level and rupture did not occur in this test (**Fig. S8b**). Since Bleb inhibits the myosin II pathway, the cell-cell adhesion junction ruptured at the initial stages and the stress level was low compared to other conditions (**Fig. S8c**).

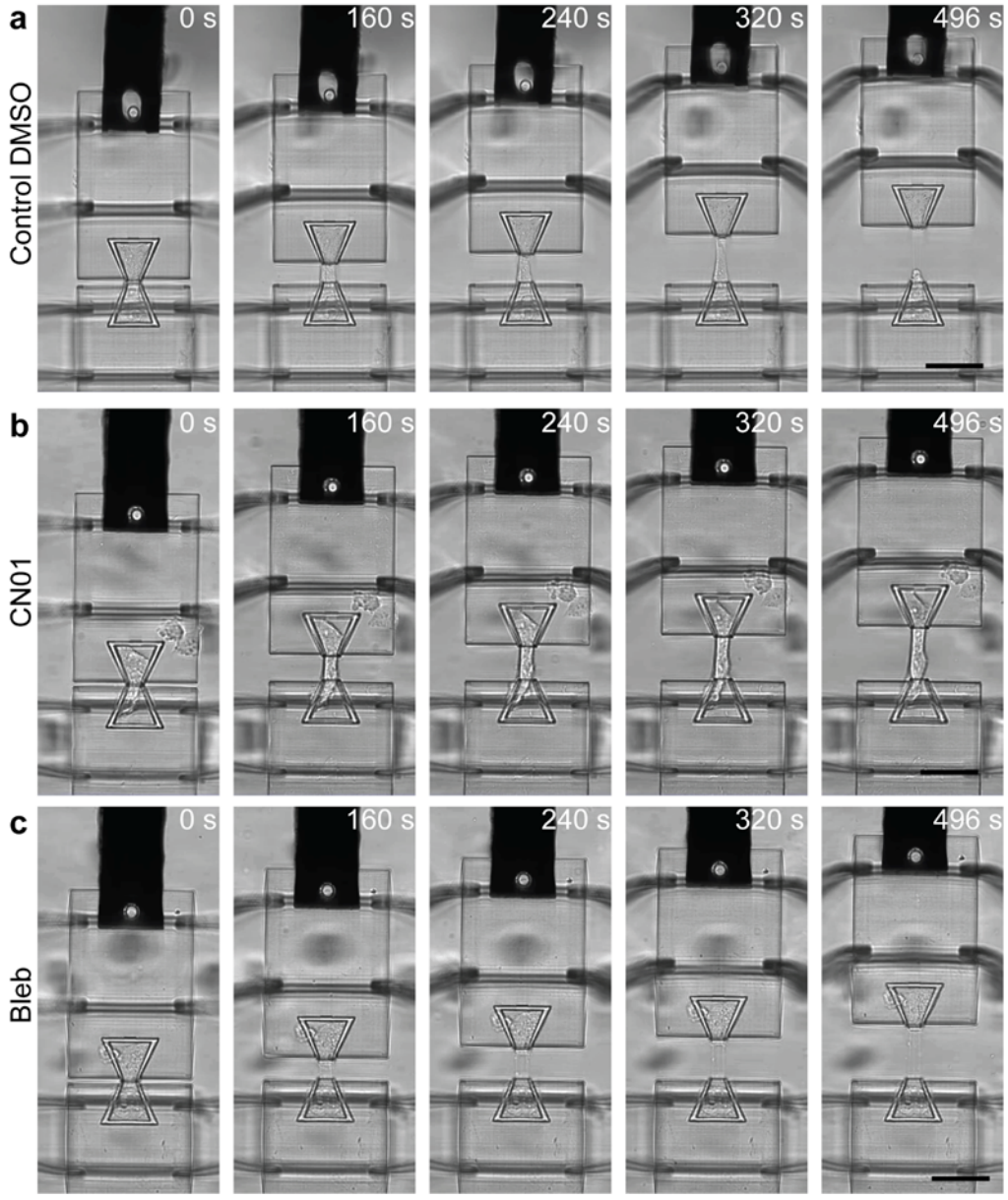

Fig. S8. Series of frames for CN01, control, and bleb under 0.005 s^{-1} strain rate stretch test. **a.** Control DMSO. **b.** CN01. **c.** Bleb. Scale bar: 50 μm.

9. Stress modulation reversal by sequential addition of contractility modulators

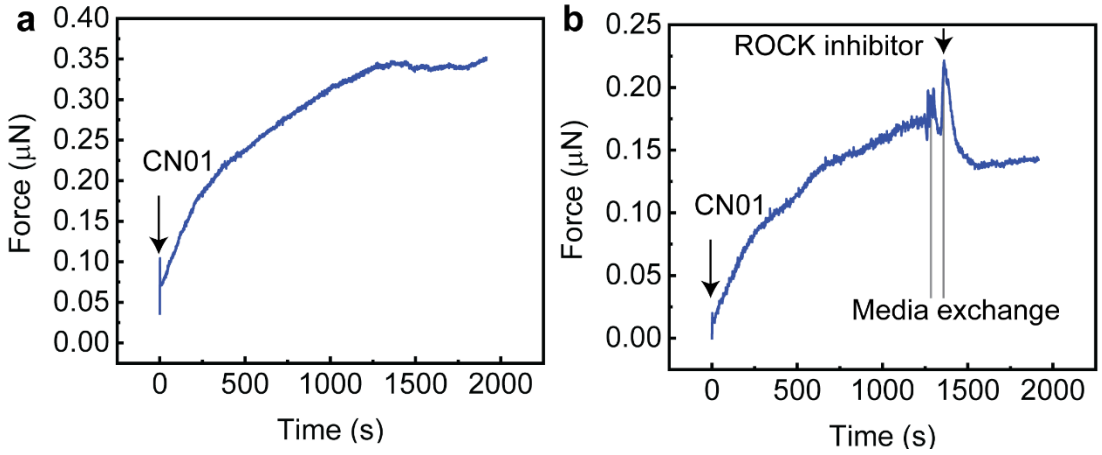

Fig. S9. Reversal of the stress modulation effect of a RhoA activator by ROCK inhibitor. a. Temporal evolution of the force sustained by a cell pair in response to CN01 (1 unit/ml) while maintaining a constant strain of 0.5. **b.** Temporal evolution of the force sustained by a cell pair in response to sequential addition of CN01 (1 unit/ml) and ROCK inhibitor while maintaining a constant strain of 0.5.

10. Cell-cell adhesion junction length calculation

To calculate the junction length, ImageJ (NIH funded software) was used. The scale is assigned to the frames of interest and a freehand line was drawn on the junction. By analyzing these lines through the software, each length can be measured and tabulated (**Fig. S10**).

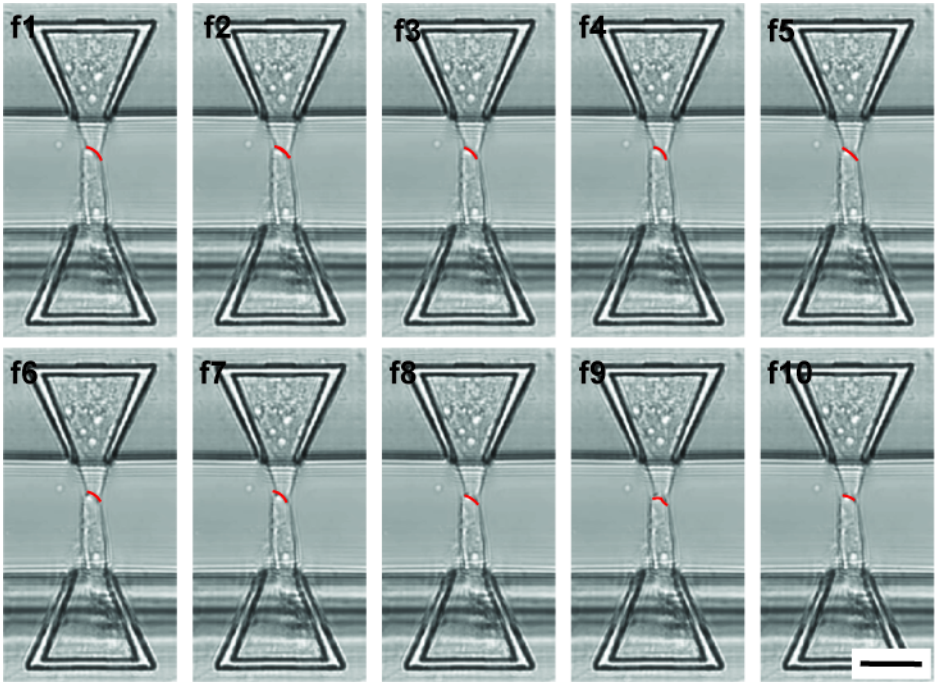

Fig. S10. Cell-cell adhesion junction length calculation. The cell-cell adhesion junction lengths were calculated using ImageJ software. After defining the scale for each frame, a freehand line was drawn on the junction and its length was captured (f1 to f10). Scale bar: 25 μm.

Table S1. **Junction length measurement on the frames in Fig. S10**.

Frame #	Junction length (μm)
1	8.019
2	7.889
3	7.931
4	7.673
5	7.043
6	6.698
7	6.121
8	5.789
9	5.513
10	5.147

11. Cadherin bond clustering in cell-cell junction under mechanical strain

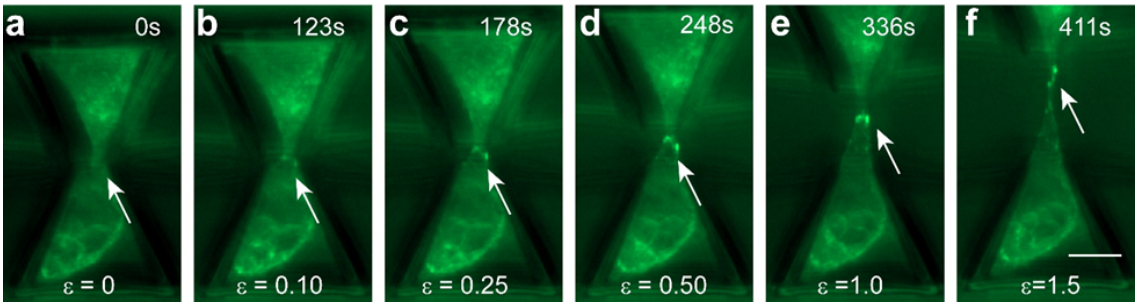

Fig. S11. E-cadherin clustering in cell-cell junction under applied strain. **a.** Under 0% strain, A431 GFP-tagged E-cadherin cells have a little expression of E-cadherin at cell-cell junction. **b-e.** As strain is increased to 10%, 25%, 50%, and 100%, respectively, E-cadherin signal increases at the cell-cell junction, indicating clustering of E-cadherin in response to stretch. **f.** At 150% strain E-cadherin begins to retract from the cell-cell contact. Scale bar: 20 μm.

12. E-Cadherin siRNA knockdown

To determine the E-cadherin bond effect on the stress-strain curve and bond rupture initiation, E-cadherin siRNA was transfected into A431 GFP-tagged E-cadherin cells. Cells were incubated with control siRNA and E-cadherin siRNA both using the Lipofectamine RNAiMAX reagent. The inhibition of E-cadherin expression was confirmed by fluorescence microscopy and immunoblotting. A knockdown of E-cadherin expression could be visualized by fluorescence microscopy after 48 h transfection. Also, immunoblotting showed that the protein levels of E-cadherin were dramatically decreased in the E-cadherin siRNA samples (48 h, 72 h, and 96 h) compared to control siRNA. These results show that E-cadherin siRNA downregulated the E-cadherin expression effectively. Note, since we used A431 cells having GFP-tagged E-cadherin, the immunoblotting showed two bands for endogenous E-cadherin (120 kDa) and GFP-tagged E-cadherin (at around 150 kDa due to the addition of GFP of 27 kDa). The control siRNA sample displayed the same two bands, and E-cadherin siRNA induced decreases in both bands. Tensile test data (**Fig. 5f-h**) compared between the control siRNA and E-cadherin siRNA.

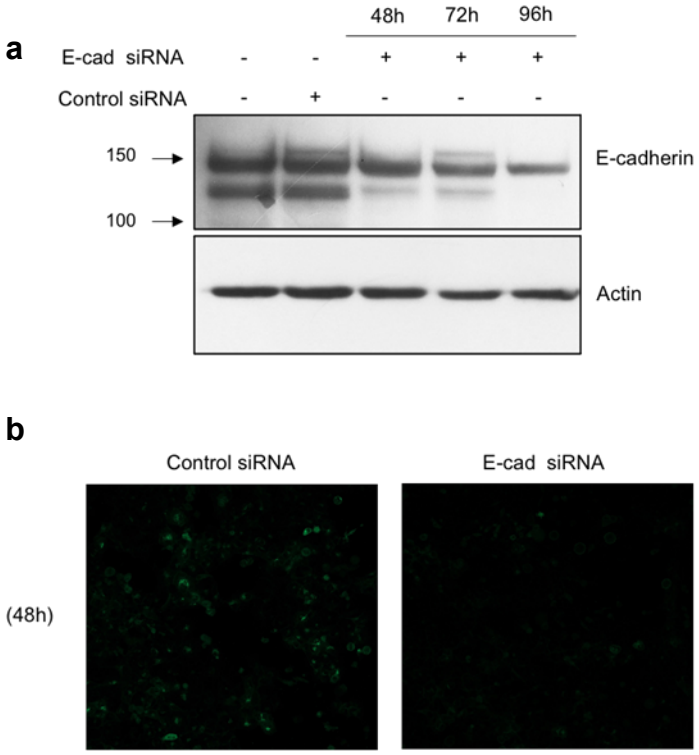

Fig. S12. Confirmation of E-cadherin siRNA silencing. **a.** A431 GFP-tagged E-cadherin cells were transfected with control siRNA or E-cadherin siRNA. After 48 h, 72 h, and 96 h post-transfection with E-cadherin siRNA, expression levels of E-cadherin were decreased in both endogenous E-cadherin (120 kDa) and GFP-tagged E-cadherin (at around 150 kDa), as assessed by immunoblot. Actin levels were not affected by the siRNA transfection. **b.** GFP signal in GFP-tagged E-cadherin A431 cells was observed after 48 h transfection with control siRNA and E-cadherin siRNA by immunofluorescence.

13. Cell-cell junction length, thickness, and nucleus-to-nucleus distance

The length of the junction is determined by measuring the length of the cell-cell contact with GFP-tagged E-cadherin, the nucleus-to-nucleus distances are calculated by examining the center-of-mass for the nucleus DAPI staining, and the thickness of cell-cell junctions are measured by examining the z-stack images of a single junction on a TPP-printed scaffold to determine the number of images in which the junction is in focus.

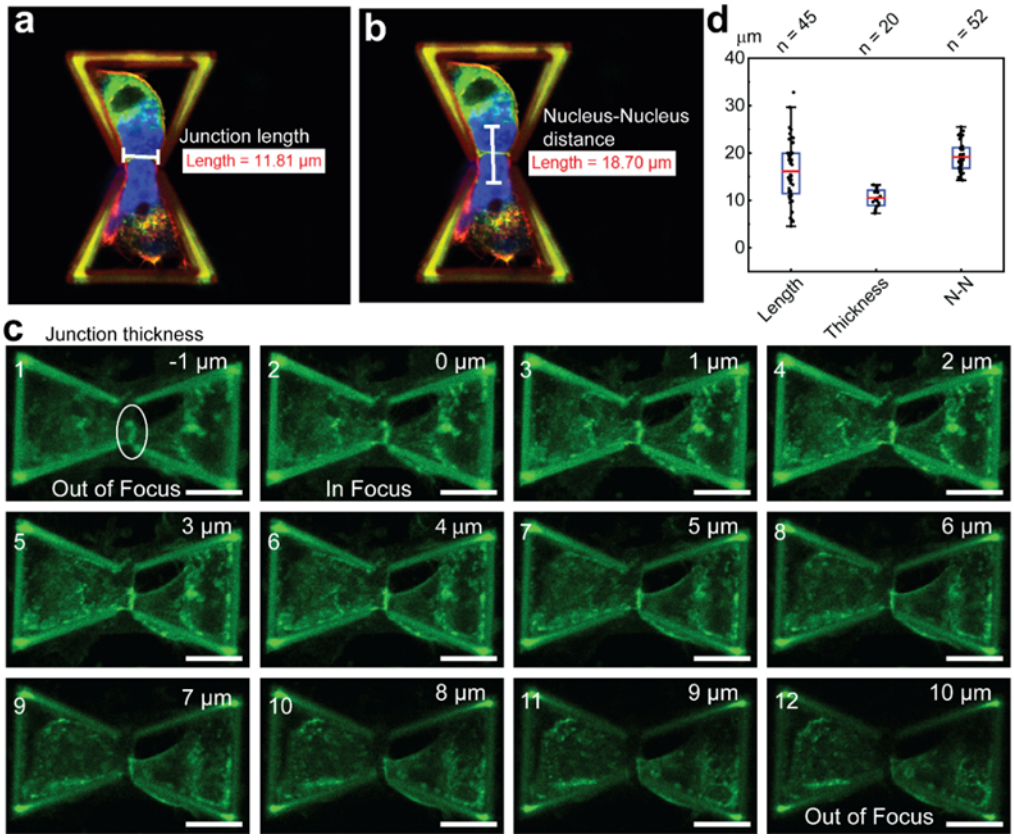

Fig. S13. Cell-cell junction dimension quantification and analysis. **a, b.** A cell pair adhered well on the device with a cell-cell junction within the gap. The junction length was measured through the junction line which is determined with the GFP-tagged E-cadherin. The nucleus-to-nucleus distances are examined by DAPI staining. **c.** Z-stack images of a cell-cell junction for thickness measurement (scale bar = 20 μm). To determine the junction thickness, cells were deposited in bowtie structures and allowed to form junctions overnight. Then, z-stack images were taken of each bowtie structure with a cell-cell pair with a spacing of 1 μm between each image. To find the thickness of the junction, the image with the bottom of the junction in focus was determined, and then each image after was examined until the top of the junction was just out of focus. From here the thickness was determined based on the number of images between these identified images (from 2 to 12). Based on the new values, we changed our assumption for the junction area in stress calculation and recalculated all previous data. **d.** Cell-cell junction length, thickness, and the nucleus-to-nucleus distance were measured and plotted (n = 45 for junction length measurements, n = 20 for thickness measurements, and n = 52 for nucleus-to-nucleus (N-N) distance measurements).

14. Initial length for strain calculation

We chose to define the initial length as the distance between the nuclei based on some observations during the stretching process. We observed that regions of the cell nearest to the junction deformed the most, while regions behind the nucleus remained relatively unmoved. To show that the region behind the nucleus is almost intact during the stretch test, we analyzed the change in displacement of a distinctive spot as a marker with respect to the edge of the bowtie, $L_M(t)$, and compared it with the displacement difference of the two movable islands, $L(t)$. As shown by the representative frames of a stretch test example, the marker, approximately in the region of the cell nucleus, was displaced only slightly from its original position relative to the edge of the bowtie ($L_M(0)$) and the maximum $L_M(t)$ reaches only 1.8 μm as compared to the maximum of $L(t)$ at 47.5 μm. Therefore, we assumed that the cell is fully anchored behind the nucleus, and while there may be some adhesions on the side near the junction, the majority of the deformation happens in this region, and these adhesions are most likely ruptured first, making this assumption more accurate. We do understand this assumption is not perfect and that there are a number of confounding factors to introduce error into the strain calculation. However, under large deformation (as the deformation of the cell pair during the stretch can reach several folds of the initial length), the influence of these errors on the calculated stress-strain relationships is mitigated.

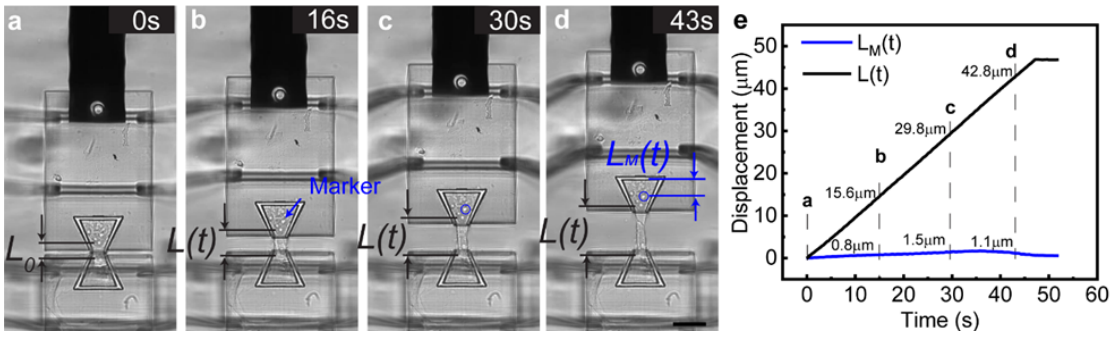

Fig. S14. Initial length calculation. a-d. Selected frames from an example stretch test showing the displacement of the upper island with respect to the lower island, $L(t)$, and the displacement of a marker close to the nucleus of the cell on the upper island with respect to the edge of the bowtie, $L_M(t)$. **e.** Plot of the displacement change over the course of the stretch test for $L(t)$ and $L_M(t)$. Scale bar = 20 μm.

Supplemental video captions:

Movie S1 (separate file).
Video recordings for the stretch test shown in Figure 3 a-b in the main text

Movie S2 (separate file).
Video recordings for the stretch test shown in Figure 3 c-d in the main text

Movie S3 (separate file).
Video recordings for the stretch test shown in Figure 3 e-f in the main text

Movie S4 (separate file).
Video recordings for the stretch test shown in Figure 3 g-h in the main text